Journal of Materials Chemistry A

Accepted Manuscript

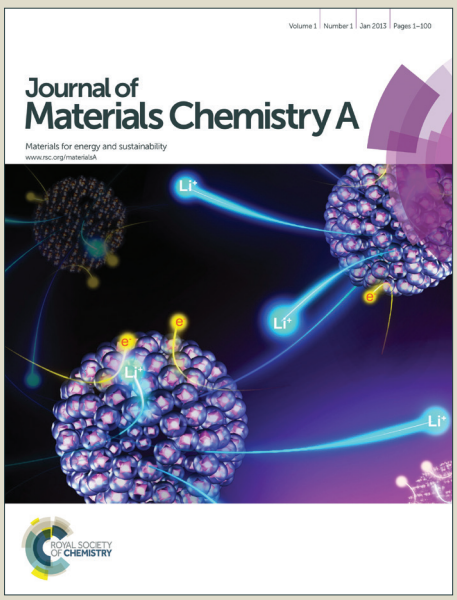

ROYAL SOCIETY OF CHEMISTRY

www.rsc.org/materialsA

Modulating the Li^+/Ni^{2+} replacement and electrochemical performance optimizing of layered lithium-rich $Li_{1.2}Ni_{0.2}Mn_{0.6}O_2$ by minor Co dopant

Xiaolan Huang, Min Wang* and Renchao Che*

Abstract

The influences of the Li^+/Ni^{2+} replacement modulated by minor Co dopant on cyclic capacity and rate performance of lithium-rich cathode material $Li_{1.2}Ni_{0.2-z/2}Mn_{0.6-z/2}Co_zO_2$ (z=0, 0.02, 0.04, 0.10) were investigated from the microstructural point of view by comprehensive techniques of high-resolution transmission electron microscopy (HRTEM) imaging, atomic-resolution electron energy loss spectroscopy (EELS), selected-area electron diffraction (SAED), and X-ray diffraction (XRD). It is found that Co played a vital role in decreasing the Li^+/Ni^{2+} replacement ratio in the hexagonal layered $Li_{1.2}Ni_{0.2-z/2}Mn_{0.6-z/2}Co_zO_2$ ($R\bar{3}m$), which is closely related to the electrochemical performance. An evident cationic ordering in the transition metal layers and stacking sequence vertical to the Li^+ diffusion orientation were observed from $Li_{1.2}Ni_{0.2-z/2}Mn_{0.6-z/2}Co_zO_2$ (z>0) system rather than $Li_{1.2}Ni_{0.2}Mn_{0.6}O_2$ system. Compared with $Li_{1.2}Ni_{0.2}Mn_{0.6}O_2$, $Li_{1.2}Ni_{0.18}Mn_{0.58}Co_{0.04}O_2$ showed excellent electrochemical performance with discharge capacity increased to 288.3 $mAhg^{-1}$ from 166.3 $mAhg^{-1}$, capacity retention improved to 98.6% from 73.9% at a current density of 0.1C after 40 cycles, and capacity enhanced to be 161.4$mAhg^{-1}$ from 113 $mAhg^{-1}$ at a higher rate of 2C. The largest interlayer spacing(0.218 nm of O-Li-O layer), highest component of Mn^{4+} ion and the most remarkable superstructure diffraction spots were found from $Li_{1.2}Ni_{0.18}Mn_{0.58}Co_{0.04}O_2$ instead of other specimens confirmed by XRD refinement, EELS, HRTEM, and SAED. Three superstructure vectors modulated by $1/4\vec{\mathbf{q}}$, $2/4\vec{\mathbf{q}}$, $3/4\vec{\mathbf{q}}$ ($\vec{\mathbf{q}}$ =[$0\bar{1}1$]) were simultaneously observed from $Li_{1.2}Ni_{0.18}Mn_{0.58}Co_{0.04}O_2$, indicating a high-degree ordering. Our findings might shed new insights into the understanding of the Li^+/Ni^{2+} replacement by doping minor amount of Co for optimizing the electrochemical performance in Li-ion batteries cathode material from the microstructural point of view.

1. Introduction

Lithium-rich manganese-based oxides such as $xLi_2MnO_3 \cdot (1-x)LiMO_2$ (M=Ni, Co, Cr, and/or Fe……) have been attracting extensive attention as modern lithium-ion battery cathode materials for their high capacity of over 250mAh g^{-1} when charged to 4.5V or higher, and giving great promise for being used in the field of electric and hybrid electric vehicles.[1-5] At present, however, there still remains great technological challenges for $xLi_2MnO_3 \bullet (1-x)LiMO_2$ to satisfy the electrochemical performance requirements of electrically powered transportation. As a typical lithium-rich manganese-based oxides cathode materials, $0.5Li_2MnO_3 \cdot 0.5LiNi_{0.5}Mn_{0.5}O_2$ (i.e.,

$Li[Li_{0.2}Ni_{0.2}Mn_{0.6}]O_2$) has raised hot interests due to its simple composition and a higher capacity coming from a higher hopping rate when Li^+ diffuse from site to site during the charge-discharge process.[6] However, it encounters the disadvantages of large irreversible capacity loss in the first cycle, rapid capacity fading and poor rate capability, which prevent them from extensive applications.[7, 8] Many researchers have drawn lots of efforts to solve these problems. Surface treatment on the $Li[Li_{0.2}Ni_{0.2}Mn_{0.6}]O_2$ were carried out such as coating on the surface of the pristine powder by ZnO,[9] MnO_2,[10] $Al(OH)_3$,[11] $LiMnPO_4$,[12] nitriding of the surface,[13] forming cubic spinel phase on the surface.[14] Moreover, $Li[Li_{0.2}Ni_{0.2}Mn_{0.6}]O_2$ with adjustable morphologies such as hollow spheres,[15] nanoplate,[16] nanorod,[17] and nanowire[18] were synthesized to improve the reversible capacity and rate capability. Yet the electrochemistry performance of xLi_2MnO_3•*(1-x)* $LiNi_{0.5}Mn_{O.5}O_2$ modified by the methods mentioned above is still limited. Partially substitution for Ni and/or Mn sites has been investigated utilizing dopants such as Cr,[19] Al,[20] Ti[21] and Y[22] to increasing the electrical conductivity, lowering the charge transfer resistance and improving the capacity retention ratio. Wang and coworkers employed chromium as a dopant in $Li[Li_{0.2}Ni_{0.2}Mn_{0.6}]O_2$ to improve the rate capability by 18% at 1.5 C rate owing to the reduced resistance of the electrode during cycling.[19] Chen and coworkers introduced yttrium dopant into $Li[Li_{0.2}Ni_{0.2}Mn_{0.6}]O_2$ to achieve a high cyclic capacity of 240.7 $mAhg^{-1}$ after 40 cycles at 0.1C rate and superior rate capability of 184.5$mAhg^{-1}$ after 40 cycles at 1C rate due to the expanded Li^+ diffusing channels by Y^{3+} dopant.[22] But the intrinsic causes of the improved electrochemical performance of $Li[Li_{0.2}Ni_{0.2}Mn_{0.6}]O_2$ by doping still remain unclear. Li^+/Ni^{2+} replacement is previously considered as a significant impact on the crystal structure because it deteriorates the electrochemical reactivity and inhibits the performance especially capacity to its full extent. [23-26]

However, the mechanism governing the influences of Li^+/Ni^{2+} replacement ratio on the electrochemical performance of $Li[Li_{0.2}Ni_{0.2}Mn_{0.6}]O_2$ system is still unclear, especially from the microstructural point of view. Li^+/Ni^{2+} replacement, referring to the displacement between the nickel ions at 3a Wyckoff site and lithium ions at 3b Wyckoff site in layered lithium metal oxide(Fig.1), always exists in $Li[Li_{0.2}Ni_{0.2}Mn_{0.6}]O_2$ and couldn't be avoided.[6] Co-doping is an effective way to improve the Li^+/Ni^{2+} replacement and enhance the rate capability of $Li[Li_{0.2}Ni_{0.2}Mn_{0.6}]O_2$ system. However, large amount of Co involved in the cathode compounds will be limited in large scale batteries for hybrid automotive applications because of its high cost, limited availability and toxity,[27, 28] Hence, there is a great need to optimize the content of Co dopant in $Li[Li_{0.2}Ni_{0.2}Mn_{0.6}]O_2$ system so as to get the best cyclic capacity and rate performance.

In this work, a series of $Li_{1.2}Ni_{0.2-z/2}Mn_{0.6-z/2}Co_zO_2$ (z=0, 0.02, 0.04, 0.10) with adjustable concentration of Co dopant at the Ni/Mn site were successfully synthesized. The optimized amount of Co dopant (z= 0.04) with an

initial discharge capacity of 288.3 $mAhg^{-1}$ and capacity retention of 98.6% after 40 cycles at 0.1C has been discovered. XRD and SQUID analysis demonstrated a larger interlayer spacing of O-Li-O (0.2181 nm) and a lower Li^{+}/Ni^{2+} replacement ratio (2.1%) in $Li_{1.2}Ni_{0.18}Mn_{0.58}Co_{0.04}O_2$(z4); HRTEM, SAED and EELS analysis confirmed more ordered stacking sequence along [001] orientation and more evident superstructure ($1/4\vec{\mathbf{q}}$, $2/4\vec{\mathbf{q}}$, $3/4\vec{\mathbf{q}}$ ($\vec{\mathbf{q}}$ =[0 $\bar{1}$1])) in addition to higher Mn average oxidation state. Our work might be helpful to understand the associations between the Li^{+}/Ni^{2+} replacement and electrochemical properties of $Li[Li_{0.2}Ni_{0.2}Mn_{0.6}]O_2$ system with minor Co dopant from a microstructural point of view.

2. Experiment

2.1 Synthesis

A facile carbonate co-precipitation associated with one-step sintering method was used in the synthesis of the pristine powder. Firstly, the stoichiometric amount of $NiSO_4$, $MnSO_4$ and/or $CoSO_4$ were added into deionized water at the same time to get a 0.2 M mixed aqueous solution (the molar ratio of transition metals is determined by the chemical formula $Li_{1.2}Ni_{0.2-z/2}Mn_{0.6-z/2}Co_zO_2$, where z is equal to 0, 0.02, 0.04, 0.10, respectively), then the mixed solution was pumped into 1 M $NaHCO_3$ aqueous solution with a suitable injection speed of 180 ml/h controlled by the Dual-channel trance syringe pump. We adjust and keep the PH of the mixed solution around 8 using balanced amount of ammonium hydroxide. After stirring for 12 hours and aging for 1 hour, the precipitate was filtered and washed with deionized water successively several times and then dried in a vacuum oven at 80℃ overnight. Then, the light green or purple powder was obtained. Secondly, the carbonate precursor mixed with a stoichiometric amount of Li_2CO_3 (5% excess for the evaporation of Li in high sintering temperature) was grounded with an agate mortar for 15 minutes, transferred into a porcelain crucible, sintered in a muffle at 500℃ for 5h and 850℃ for 10h, and cooled naturally in the muffle to the room temperature.

2.2 Characterization

The morphology of the powders was acquired on a (S-4800, HITACHI) field-emission scanning electron microscope operated at 1.0 kV. Energy dispersive X-ray spectroscopy (EDX) was operated at 20.0 kV to characterize the existence, ratio and distribution of the transition metal ions. The crystal structures of the as-made powders were obtained using an X-ray diffractometer (Brucker, D8 ADVANCED) with Ni-filtered Cu-Kα radiation (40 kV, 40 mA). Data were collected over the 2θ range of 10~70° with a scan rate of 4° /min. XRD refinement was conducted by the Rietveld method using TOPAS program (DIFFRAC TOPAS 4.2). To get more detailed structural information, high-resolution TEM (HRTEM), selected-area electron diffraction (SAED) and

electron energy loss spectroscopy (EELS) patterns were performed on a JEOL JEM-2100F transmission electron microscope equipped with a post-column Gatan imaging filter (GIF-Tridium) at an acceleration voltage of 200 kV. EELS data were recorded with a two-dimensional back-illuminated charge-coupled device camera (Gatan-894, 2k×2k) with a low read-out noise and a negligible dark count noise, and the dispersion is 0.3 eV per channel for monitoring the fine structure changes of oxygen and transition metal ions and 0.03 eV for collecting the spectra of Li^+ in the range of 40~100 eV. The digital micrograph software (Gatan) was used for image recording/processing.

Magnetic properties were determined with a SQUID VSM (Superconducting QUantum Interference Device, Vibrating Sample Magnetometer, from the Quantum Design Company, USA). The temperature dependences of the magnetic susceptibility were measured on cooling the specimens from 300K to 2K in a magnetic field of 10k Oe. Magnetic curves M(H) have been measured in an applied magnetic field in a range of 0~30k Oe.

Electrochemical performance measurements were carried out using R2016 coin-type cells. To assemble the coin-type cell, the as-prepared power was thoroughly mixed with carbon black (super-P), polyvinylidene difluoride(PVDF) in N-methyl-2-pyrrodine(NMP) solvent by the mass ratio of 8:1:1 to get a black slurry. Then casted the slurry onto an aluminum foil current collector, punched them into disks with a diameter of 12 mm after drying the slurry-casted foil in an vacuum oven at 80℃ for 12 hours. R2016 coin-type cells were then assembled in an argon-filled dry glove box with the metallic lithium plate as the anode, and the Celgard 2400 membrane as a separator. The electrolyte solution was 1M $LiPF_6$ electrolyte in ethylene carbonate/diethyl carbonate (EC/DEC, 1:1 by volume). The cyclic and rate performance were measured using a Land testing system in galvanostatic mode in the voltage range of 2.0~4.8V. A.C. Impedance spectrum were conducted on the CHI604D electrochemical workstation with an amplitude of 5 mV in the frequency range of 100 kHz to 0.01 Hz.

3. Results and discussion

3.1. Morphology and crystal structure

The morphology and particle size of the specimens $Li_{1.2}Ni_{0.2-z/2}Mn_{0.6-z/2}Co_zO_2$ with z=0, 0.02, 0.04 and 0.10 (hereafter using z0, z2, z4, z10 for short) are shown in Fig.2. The as-made powders are consisted of small sub-micron polyhedron particles, and their average sizes are 0.150, 0.233, 0.234, 0.163 μm, respectively (diameter distribution histograms in Fig.2 insets). With increasing Co dopant content in the specimen, the degree of aggregation decreased and the size uniformity of the particles enhanced. EDX data demonstrated that experimental ratio of different types of transition metal ions (Ni, Co and Mn) in the as-prepared sample was consistent with that of stoichiometric ratio (Table S1 and Fig.S1).

Fig. 3(a) is the XRD pattern of the as-made powder. All major peaks can be well indexed according to hexagonal $R\bar{3}m$ space group (α-$NaFeO_2$). The peaks (006)/(012) and (108)/(110) are well separated into doublets in the range of 36.5~39°and 64~65.5°. The magnification of the weaker peaks between 20~25°(Fig.3b) indicated the existence of superstructure (C2/m).[29, 30] A small right shift in the XRD pattern, which is more briefly reflected by a small decrease of cell parameter **a** and **c** (Table 1) with the increase of Co dopant, confirmed the successful doping of Co into the Ni/Mn site in the transition metal layers. This can be explained by Co^{3+} (γ=0.54Å) has a similar ion radius with Mn^{4+} (γ=0.53Å), but smaller than that of Ni^{2+} (γ=0.69Å).[27] The integrated intensity ratio of (003) to (104) peaks, $I_{(003)}/I_{(104)}$, is considered as a sensitive parameter to determine the cationic distribution in the α-$NaFeO_2$-type lattice, The smaller $I_{(003)}/I_{(104)}$ is, the higher structural deviation from hexagonal towards cubic symmetry and worse cationic distribution.[31] The specimen z4 has the largest $I_{(003)}/I_{(104)}$ value of 1.965 among all the specimens (Table 1), indicating the best cationic distribution, which can also be proved by HRTEM and SAED directly.

To further study the cationic distribution and the microstructure, Li^+/Ni^{2+} replacement was studied by conducting refinement on TOPAS program (Table 1 and Fig.S2). The Ni^{2+}(3b) (Table 1), which is the amount of Ni^{2+} appeared in the Li layer, indicates the Li^+/Ni^{2+} replacement ratio. The percentage of Ni^{2+}(3b) from the total Ni^{2+} in per chemical formula unit was also calculated by taking into account of the small difference in the total amount of Ni^{2+} in each specimen. Both the Ni^{2+}(3b) and Ni^{2+} % decreased obviously with the increase of Co dopant, which claimed the great effect of Co dopant on modulating the Li^+/Ni^{2+} replacement. In addition, the interlayer spacing (I_{LiO2}) varied as the Co content increased: increased at first, and then decreased. Because Ni^{2+} (γ=0.69Å) has a slightly smaller cation radius than that of Li^+(γ=0.72Å),[27] the sample with a lower Li^+/Ni^{2+} replacement ratio has a higher occupancy of Li^+ in the lithium layer with a higher I_{LiO2}. For the specimen z10 with excessive Co dopant, I_{LiO2} decreased on the contrary due to the much longer bond length of Co^{3+} (χ_p=1.88) than that of Mn^{4+} (χ_p =1.55). Li^+ diffuses perpendicular to the [001] direction in the layered lithium rich metal oxide.[4, 32] The large interlayer spacing of oxygen-lithium-oxygen (I_{LiO2}) facilitates Li^+ diffusion in the (001) plane and intercalate/deintercalate during the charge/discharge process with decreased hindrance, therefore, a better electrochemical performance can be expected.[6]

3.2 Magnetic susceptibility

Magnetic properties were tested to further investigate the effect of Li^+/Ni^{2+} replacement modulated by Co in

the specimens from the perspective of nanoscopic scale. The temperature dependences of magnetic susceptibility (Fig.4a) indicate an antiferromagnetic behavior in accordance with those reported by Zheng [33] and Mohanty.[34] A paramagnetic behavior above 150K can be observed and the magnetization varies linearly with the applied magnetic field. The linear variations of the reciprocal magnetic susceptibility χ^{-1} with T can be described by Curie-Weiss Law. (χ^{-1}=H/M, H is the magnetic field and M is the magnetization, Fig.4a inset).

The magnetic parameters and the amount of Ni^{2+} (3b) calculated by fitting χ^{-1}(T) above 150K using Curie-Weiss Law[34, 35] for the specimen z0, z2, z4, z10 are shown in Table S2. The results obtained from magnetic analysis were in agreement with those by Rietveld refinement. The Curie temperature and the effective moment μ_{exp} decrease with the increase of Co dopant content, which can be attributed to the super-exchange interaction of transition metal ions. Due to the Li^{+}/Ni^{2+} replacement, Ni^{2+} (3b) creates a new super-exchange path with Ni and Mn in the transition metal layers (Ni^{2+}(3a), Mn^{4+}(3a)) via a bonding angle of 180°, and the strong Ni^{2+}(3a)-O-Mn^{4+}(3a) (antiferromagnetic, AFM) and weak Ni^{2+}(3a)-O-Ni^{2+}(3a) (ferromagnetic, FM) couplings are partially replaced by strong Ni^{2+}(3b)-O-Mn^{4+}(3a) (FM) and more strong Ni^{2+}(3b)-O-Ni^{2+}(3a) (AFM) couplings[35], leading to a much strong antiferromagnetic property and high effective magnetic moment μ_{exp}.[24] With the decreasing of the Li^{+}/Ni^{2+} replacement ratio, the effective magnetic moment decreased. In addition, when Co dopant involved in $Li_{1.2}Ni_{0.2}$ $Mn_{0.6}O_2$, Co^{3+} was diamagnetic in the $3d^6$-LS configuration, and magnetic dilution occurred.[36] The transition temperature θ_p and the effective magnetic moment $\mu_{exp.}$ decreased for the discontinuity of magnetic percolation. Compared with the specimen z0, the θ_p and μ_{exp} of z10 reduced to 22.4 K and 2.99μ_B from 28K and 3.19μ_B, respectively. Therefore, the replacement of partial Mn and Ni by Co can inhibit the effect of Li^{+}/Ni^{2+} replacement, which can also be verified by Ni^{2+} (3b). The discrepancy between μ_{exp} and $\mu_{theor.}$ in the Table S2 can be explained by the reduction of Mn and/or oxidation of Ni in the as-prepared material. Since the presence of Ni^{3+} may break the electro neutrality of the compound, the only possible choice is to assume that the Mn is in a mixed state of Mn^{4+} and Mn^{3+},[37] which can be further proved by EELS analysis.

3.3 Microstructure analysis

The different microstructural features generated from the four specimens with diverse degree of Li^{+}/Ni^{2+} replacement were directly imaged by HRTEM. A layer spacing of ~4.7 Å along the [003] direction has been observed from all specimens, indicating perfect layered structure resulted from our synthesis. In addition, an extra structure can be observed on the margin of the particle in specimen z0. As denoted by the yellow dashed line in Fig.5(a) and Fig.S3, the region on the left has a interlayer spacing of 0.24 nm and its FFT (Fast Fourier

Transformed) images indicate a monoclinic C2/m structure which is different from the inner hexagonal $R\bar{3}m$ structure on the right. Additional columns of transition metals(yellow line) have been added between the original transition metal columns (green lines) which may lead to a negative effect on the diffusion of Li^+ inside the particle. Contrast line-scanning profiles (Fig.5 inset) of each cationic column marked by the red dotted boxes were obtained perpendicular to the [003] direction. The increasing intense uniformity in the contrast profile indicated a more ordered sequence of cations arranged in the transition metal layers with the decrease of the Li^+/Ni^{2+} replacement ratio. The specimen z0, with the highest Li^+/Ni^{2+} replacement ratio among the four specimens, was directly observed by the atomic level EELS analysis. The EEL spectra were acquired on a single atom with dark contrast in the transition metal layer marked by blue circle and atom with brighter contrast in the lithium layer marked by the yellow circle in the specimen z0 (Fig.5e), respectively. Taking into account of the plasmon effects contributed from the whole lattice, an energy dispersion of 0.03 eV was used in collecting the energy loss spectrum in a range of 40~100 eV, the peaks between 50~60 eV and 65~72 eV might come from the transition metal' M edges (Ni-M, Mn-M), and the peak in the range of 60~63.5 eV might be indexed to the Li-K edge in the transition metal layers (Fig.5f).[38] Energy loss peaks around 860 eV could be indexed to Ni element in the lithium layer (Fig.5g) With the decrease of Li^+/Ni^{2+} replacement ratio modulated by Co dopant, the stacking sequence (Fig.5) along the [003] direction become more well-aligned, especially in the specimen z4 and z10 shown by the orange and light blue lines (Fig.5). The orange lines correspond to the ordered $R\bar{3}m$ phase and the light blue lines present the structural defects which result from the partially ordered $R\bar{3}m$ or the mixture of $R\bar{3}m$ and C2/m phase. During the charge and discharge process, Li^+ diffuses perpendicular to the [001] direction[4, 32] marked by the red arrows (Fig.5). The more regular ion arrange in the transition metal layers and more aligned the transition metal layers stacking along the [003] direction, the less propagation resistance of Li^+ is during transportation. Hence a better electrochemical performance will be expected, which are exactly consistent with the data reported in Fig.8.

To get further evidence for the structural features mentioned above, SAED patterns were obtained by tilt each specimen to zone axis. Typical diffraction patterns along the $[1\bar{1}0]_{hex}$ zone axis are shown in Fig.6. Additional less intense diffraction spots vertical to the [110] direction can be observed (Fig.6). These less intense spots indicate the formation of a $\sqrt{3}a_{hex}\times\sqrt{3}a_{hex}$ superstructure in the transition metal layers,[27, 29] which can also be proved by the more intense peak in XRD at the range of 20~25 (Fig.3b).The diffraction spots are elongated to diffuse streaks as pointed out by red arrow(Fig.6a) in the specimen z0 ($Li_{1.2}Ni_{0.2}Mn_{0.6}O_2$). As the Li^+/Ni^{2+} replacement ratio decrease in the specimen, the additional diffraction spots become more distinguishable. This transformation from

streaks to distinguishable spots among these main diffraction spots is related to the random stacking of domains with different zone axes such as [$1\bar{1}0$], [100], [110] that present different thicknesses or planar defects.[39, 40]

Herein, the specimen, which had lower Li^+/Ni^{2+} replacement ratio (z4), had a more ordered ion arrangement in the transition metal layers. Extra weaker diffraction streaks marked by the yellow dotted box and the corresponding enlarged view on the top right of each picture (Fig.6) can be observed parallel to [00l], indicated the existence of super-stacking-sequence of transition metal layers stacking along the [00l] direction, which keep accordance with the results from the HRTEM image.

Similar superstructure can also be observed with the electron incidence parallel to the $[100]_{hex}$ (Fig.7). The basic modulation was defined as a wave vector with $\vec{\mathbf{q}} = (0\bar{1}1)$. The additional weaker diffraction spots at the systematic positions of $1/4\ \vec{\mathbf{q}}$, $2/4\ \vec{\mathbf{q}}$, $3/4\vec{\mathbf{q}}$ (Fig.7c) and $1/2\vec{\mathbf{q}}$ (Fig.7d) belong to the superstructure due to cationic ordering. More briefly diagram was depicted in Fig.7 (e ~h). Quite different superstructure modulation spots are shown between the main diffraction spots. No superstructure spots could be observed in the specimen z0 and z2, and only one superstructure spots detected in the specimen z10, however, the specimen z4 has three modulation periods ($1/4\vec{\mathbf{q}}$, $2/4\vec{\mathbf{q}}$, $3/4\vec{\mathbf{q}}$), indicating a perfect periodicity of the transition metal ions which further confirmed the highest cationic ordering and stacking sequence in the specimen z4 mentioned above.

EELS can give information about the elemental composition, valence state and interaction among the transition metals. Herein, the ex situ EELS data were collected to give quantified proof for the electronic structure and direct explanations of the differences of interaction and electronic environment in the specimens from the microstructural point of view. For all the specimens, the oxygen K edge is dominated by two peaks (Fig.8a), and energy loss around 532eV marked as α is attributed to the transition from 1s oxygen core state to the 2p state hybridized with manganese 3d orbitals. The peak β is related to the unoccupied oxygen 2p states hybrid with manganese 4s and 4p.[39, 41] The more hybridization between the O 2p orbit with the manganese 3d orbit, the orbital electron cloud among the two core will be more homogenous. herein the energy separation between the (α) and (β) can reflect the transition metal oxidation state such as the manganese: the smaller of the E(β)-E(α), the lower the oxidation state is.[41] The energy separation between the peak α and the main peak β are 11.08, 11.28, 11.38, 11.36 eV, respectively, so we can predict a higher oxidation of Mn in the specimen z4. The Mn L_2, L_3 edges, which is corresponding to transitions from the 2p1/2 and 2p3/2 to empty 3d orbital, can demonstrate the atomic-like "white-line" features clearly. As shown in the enlarged view of Mn L_3 edge and Mn L_2 edge in Fig.8(b), the critical excitation energy of Mn L_3 edge for specimens z0, z2, z4, z10 are 644.5, 645.2, 645.7, 644.8 eV, and corresponding energy loss positions of Mn L_2 edges are 655.1, 655.6, 656.0, 655.3 eV, respectively. Compared to

the specimen z0, a small shift to the higher energy loss position for the specimens with Co dopant have been observed, indicating a higher oxidation state of Mn in Co doped specimens, especially the specimen z4[4, 42], which is consistent with the results from the analysis of the energy separation between the (α) and (β) above. Li_2MnO_3 component plays a role in stabling the layered structure of the $Li_{1.2}Ni_{0.2}Mn_{0.6}O_2$ system, especially during the charge/discharge process, in which, the oxidation state of Mn is +4. A lower average oxidation state of Mn, i.e, $Mn^{3.5+}$ will produce phase transformation due to the Jahn-Teller Effect. Herein, the highest average oxidation state of Mn in the specimen $Li_{1.2}Ni_{0.18}Mn_{0.58}Co_zO_2$ further proved the better stability during cycling which deserved a better cyclic performance.

3.4 Electrochemistry characterization

3.4.1 Cyclic and rate performance

Typical initial charge and discharge plots for the specimens cycled at a current density of 0.05C (1C=200 $mAhg^{-1}$) delivered a super high specific charge capacity of 441.4, 386.2, 403.4 and 393.8 $mAhg^{-1}$, respectively (Fig. 9a). The high capacity is due to the long plateau at about 4.5V which is a chemical reaction of the Li_2MnO_3 phase.[43] With a relatively low coulumbic efficiency in the initial cycle, an improvement of the efficiency can be observed in the Co doped case, especially the specimen z4 (inset in Fig.9a). However, there is still great space for the improvement of the coulombic efficiency in the initial cycle for all the specimens. Works aimed at improving the initial coulombic efficiency will be done in the future such as surface coating and pre-cycling treatment. Due to the modulating of Co, a much higher specific discharge capacities have been obtained after 40 cycles at a current density of 0.1C, and the specific discharge capacities were 166.34, 217, 288.3, 250.2 $mAhg^{-1}$ for z0, z2, z4, z10(Fig. 9b), which were similar or a bit higher than those reported before.[10, 11, 22] Owing to the large interlayer space of O-Li-O and ordered stacking sequence, the specimen z4 achieved a very high discharge capacity and capacity retention of 98.6%, remarkably improved from 73.9% for $Li_{1.2}Ni_{0.2}Mn_{0.6}O_2$. Fig.9 (c~d) exhibited the rate performance for z0, z2, z4, z10 at a charge and discharge rate from 0.05C to 2C and its normalized discharge capacity plot. The capacity retention performance has been improved evidently by Co doping, which is more prominent in the specimen z4. Because of the more ordered cationic ordering and higher Mn^{4+} component, the specimen z4 possesses a discharge capacity of 161.4 $mAhg^{-1}$ and capacity retention ratio of 52.9% at 2C rate, much higher than 113 $mAhg^{-1}$ and 36.3% for $Li_{1.2}Ni_{0.2}Mn_{0.6}O_2$. The specimen z10 with high Co doped content, however, showed electrochemical performance inferior to the specimen z4 because of increasing steric hindrance for Li^+ diffusion caused by less ordered transition metal stacking order, lower Mn^{4+} component and smaller

O-Li-O interlayer spacing of 2.163 Å.

3.4.2 EIS test

Electrochemical impedance spectroscopy (EIS) was conducted to get further evidence to solidify the results from the microstructure analysis. Data was collected on the CHI604D workstation after the cells were charged to 4.2V. The first semicircle in the Nyquist plot (Fig. 10(a)) from the high to middle frequency represents the internal resistance of the battery, the second semicircle from the middle to low frequency corresponds to the charge transfer resistance between the electrode and electrolyte interface, and the straight line in the low frequency attributes to the Warburg impedance to the Li^+ diffusion.[44, 45] The EIS spectrum were fitted according to the R(QR)(Q(RW)) model (Fig.S4) using the ZSimpWin software. The simulated parameters and the apparent diffusion coefficient D_{Li+} which is calculated according to those reported[46, 47] are listed in Table S3. All the Co doped specimens have a lower Rct and higher D_{Li+} than those of $Li_{1.2}Ni_{0.2}Mn_{0.6}O_2$, and the specimen z4 has the smallest Rct of 134.7 Ω and biggest D_{Li+} of 5.41×10^{-15} cm^2s^{-1} at the charge state of 4.2V which is the delitiation of Li^+ from the bulk of the particles in the specimen. Owing to the participation of Co dopant in the transition metal layer, Li^+/Ni^{2+} replacement decreased with the increase of Co dopant. The improved cationic ordering in the transition metal layers resulted in reducing steric hindrance for Li^+ diffusion and facilitating the migration of Li^+ in the transition metal layer (Fig.S5). However, as the excessive decrease of Li^+/Ni^{2+} replacement ratio, the layered structure became unstable after the delithiation because of reduction of O-Ni(3b)-O skeleton in the O-Li-O interlayer, which can inhibit then O^{2-}-O^{2-} repulsion and the shrinkage even collapse in the O-Li-O interlayer. The results of Rct and D_{Li+} were consistent with the microstructure and electrochemical property analysis above.

4. Conclusion

In summary, a series of minor Co doped lithium-rich manganese based oxide materials with a sub-micron particle size were synthesized by a facile one-step sintering method. All of the as prepared materials possessed an excellent layered hexagonal $R\bar{3}m$ structure. The specimen $Li_{1.2}Ni_{0.18}Mn_{0.58}Co_{0.04}O_2$ (z4), with an optimum Li^+/Ni^{2+} replacement of 2%, owned a stable discharge capacity of 288.3 $mAhg^{-1}$ with only 1.4% capacity fade after 40 cycles at a current of 0.1C and exhibited a capacity of 161.4 $mAhg^{-1}$ at a higher rate of 2C, according to the XRD refinement and SQUID characterization. Direct proof from HRTEM and SAED combined with EELS analysis indicated that $Li_{1.2}Ni_{0.18}Mn_{0.58}Co_{0.04}O_2$ had a better cationic ordering and stacking sequence parallel to the Li^+ diffusion plane as well as structural stability because of more Mn^{4+} involved. Doped Co had a great influence

on the cycling performance and rate capability. With the increasing Co to an optimum content, the Li^+/Ni^{2+} replacement decreased to achieve better cationic ordering, which resulted in better initial coulombic efficiency, cyclic performance and rate capability. Our work gives insights into understanding the effect of Li^+/Ni^{2+} replacement modulated by Co doping on the electrochemical properties, which can be helpful for optimizing the microstructure and improving the performance of $Li[Li_{0.2}Ni_{0.2}Mn_{0.6}]O_2$ cathode material.

Supporting Information

Supporting Information is available online or from the author.

Acknowledgements

This work was supported by the Ministry of Science and Technology of China (973 Project Nos. 2013CB932901 and 2009CB930803), and the National Natural Foundation of China (Nos. 21203033, 51172047, 50872145, 51102050 and U1330118). This project was sponsored by Shanghai Pujiang Program and "Shu Guang" project of Shanghai Municipal Education Commission and Shanghai Education Development Foundation (09SG01).

Notes and references

Department of Materials Science and Laboratory of Advanced Materials, Fudan University, Shanghai 200438, P.R. China. Fax: 86 021 51630210; Tel: 86 021 51630213; E-mail: rcche@fudan.edu.cn; Tel: 86 021 51630233; E-mail: minwang@fudan.edu.cn

1. M. Gu, I. Belharouak, A. Genc, Z. Wang, D. Wang, K. Amine, F. Gao, G. Zhou, S. Thevuthasan, D. R. Baer, J. G. Zhang, N. D. Browning, J. Liu and C. Wang, *Nano Lett.*,2012,**12**,5186-5191.
2. K. A. Jarvis, Z. Deng, L. F. Allard, A. Manthiram and P. J. Ferreira, *J. Mater. Chem.*,2012,**22**,11550-11555.
3. J. Liu, B. ReejaJayan and A. Manthiram, *J. Phys. Chem. C*,2010,**114**,9528-9533.
4. B. Xu, C. R. Fell, M. Chi and Y. S. Meng, *Energy Environ. Sci.*,2011,**4**,2223-2233.
5. K. A. Jarvis, Z. Deng, L. F. Allard, A. Manthiram and P. J. Ferreira, *Chem. Mater.*,2011,**23**,3614-3621.
6. Y. S. M. Kisuk Kang, Julien Breger, *Science*,2006,**311**,977-979.
7. Q. Y. Wang, J. Liu, A. V. Murugan and A. Manthiram, *J. Mater. Chem.*,2009,**19**,4965-4972.
8. P. He, H. Yu, D. Li and H. Zhou, *J. Mater. Chem.*,2012,**22**,3680-3695.
9. G. Singh, R. Thomas, A. Kumar, R. S. Katiyar and A. Manivannan, *J. Electrochem. Soc.*,2012,**159**,A470-A478.
10. Y. Liu, S. Liu, Y. Wang, L. Chen and X. Chen, *J. Power Sources*,2013,**222**,455-460.
11. Y. J. Kang, J. H. Kim, S. W. Lee and Y. K. Sun, *Electrochim. Acta*,2005,**50**,4784-4791.
12. Q. Q. Qiao, H. Z. Zhang, G. R. Li, S. H. Ye, C. W. Wang and X. P. Gao, *J. Mater. Chem. A*,2013,**1**,5262-5268.

13. H. Z. Zhang, Q. Q. Qiao, G. R. Li, S. H. Ye and X. P. Gao, *J. Mater. Chem.*,2012,**22**,13104-13110.
14. B. Song, H. Liu, Z. Liu, P. Xiao, M. O. Lai and L. Lu, *Sci. Rep.*,2013,**3**,doi:10.1038/srep03094.
15. Y. Jiang, Z. Yang, W. Luo, X. Hu and Y. Huang, *Phys. Chem. Chem. Phys.*,2013,**15**,2954-2960.
16. J. Cho, Y. Kim and M. G. Kim, *J. Phys. Chem. C*,2007,**111**,3192-3196.
17. J. Yang, F. Cheng, X. Zhang, H. Gao, Z. Tao and J. Chen, *J. Mater. Chem. A*,2014,**2**,1636-1640.
18. M. G. Kim, M. Jo, Y. S. Hong and J. Cho, *Chem. Commun.*,2009,218-220.
19. L. F. Jiao, M. Zhang, H. T. Yuan, M. Zhao, J. Guo, W. Wang, X. D. Zhou and Y. M. Wang, *J. Power Sources*,2007,**167**,178-184.
20. A. Dianat, N. Seriani, M. Bobeth and G. Cuniberti, *J. Mater. Chem. A*,2013,**1**,9273-9280.
21. Z. Q. Deng and A. Manthiram, *J. Phys. Chem. C*,2011,**115**,7097-7103.
22. N. Li, R. An, Y. Su, F. Wu, L. Bao, L. Chen, Y. Zheng, H. Shou and S. Chen, *J. Mater. Chem. A*,2013,**1**,9760-9767.
23. J. Xiao, N. A. Chernova and M. S. Whittingham, *Chem. Mater.*,2008,**20**,7454-7464.
24. X. Zhang, W. J. Jiang, A.Mauger, Qi Liu, F.Gendron and C.M.Julien, *J. Power Sources*,2010,**195**,1292-1301.
25. H. Yu, Y. Qian, M. Otani, D. Tang, S. Guo, Y. Zhu and H. Zhou, *Energy Environ. Sci.*,2014,1068-1078.
26. K. Lee, S. Myung, J. Prakash, H. Yashiro and Y. Sun, *Electrochim. Acta*,2008,**53**,3065-3074.
27. H. Koga, L. Croguennec, P. Mannessiez, M. Ménétrier, F. Weill, L. Bourgeois, M. Duttine, E. Suard and C. Delmas, *J. Phys. Chem. C*,2012,**116**,13497-13506.
28. Y. Sun, D. Lee, Y. J. Lee, Z. Chen and S. Myung, *ACS Appl. Mater. Interfaces*,2013,**5**,11434-11440.
29. Y. S. Meng, G. Ceder, C. P. Grey, W. S. Yoon, M. Jiang, J. Bréger and Y. Shao-Horn, *Chem. Mater.*,2005,**17**,2386-2394.
30. M. M. Thackeray, S.-H. Kang, C. S. Johnson, J. T. Vaughey, R. Benedek and S. A. Hackney, *J. Mater. Chem.*,2007,**17**,3112-3125.
31. J. Wang, M. Zhang, C. Tang, Y. Xia and Z. Liu, *Electrochim. Acta*,2012,**80**,15-21.
32. G. Wei, X. Lu, F. Ke, L. Huang, J. Li, Z. Wang, Z. Zhou and S. Sun, *Adv. Mater.*,2010,**22**,4364-4367.
33. Z. Li, N. A. Chernova, J. Feng, S. Upreti, F. Omenya and M. S. Whittingham, *J. Electrochem. Soc.*,2012,**159**,A116-A120.
34. D. Mohanty, S. Kalnaus, R. A. Meisner, A. S. Safat, J. Li, E. A. Payzant, K. Rhodes, I. I. I. D. L. Wood and C. Daniel, *Rsc Adv.*,2013,**3**,7479-7485.
35. M. M. Natasha A.Chernova, Jie Xiao,M.Stanley Whittingham,Julien Breger,Clare P.Grey, *Chem. Mater.*,2007,**19**,4682-4693.
36. N. Kawai, T. Nakamura, Y. Yamada and M. Tabuchi, *J. Power Sources*,2011,**196**,6969-6973.
37. L. Simonin, J.-F. Colin, V. Ranieri, E. Canévet, J.-F. Martin, C. Bourbon, C. Baehtz, P. Strobel, L. Daniel and S. Patoux, *J. Mater. Chem.*,2012,**22**,11316-11322.
38. J. Zheng, M. Gu, J. Xiao, P. Zuo, C. Wang and J.-G. Zhang, *Nano Lett.*,2013,**13**,3824-3830.
39. A. Boulineau, L. Simonin, J.-F. Colin, E. Canévet, L. Daniel and S. Patoux, *Chem. Mater.*,2012,**24**,3558-3566.
40. A. Ito, D. C. Li, Y. Sato, M. Arao, M. Watanabe, M. Hatano, H. Horie and Y. Ohsawa, *J. Power Sources*,2010,**195**,567-573.
41. G. H. Du, Z. Y. Yuan and G. Van Tendeloo, *Appl. Phys. Lett*,2005,**86**,063113-063113-3.
42. H. Tan, J. Verbeeck, A. Abakumov and G. Van Tendeloo, *Ultramicrosc.*,2012,**116**,24-33.
43. A. R. Armstrong, M. Holzapfel, P. Novák, C. S. Johnson, S.-H. Kang, M. M. Thackeray and P. G. Bruce, *J. Am. Chem. Soc.*,2006,**128**,8694-8698.
44. X. Zhang, D. Luo, G. Li, J. Zheng, C. Yu, X. Guan, C. Fu, X. Huang and L. Li, *J. Mater. Chem. A*,2013,**1**,9721-9729.

45. J. M. Zheng, X. B. Wu and Y. Yang, *Electrochim. Acta*,2011,**56**,3071-3078.

46. X. Wang, H. Hao, J. Liu, T. Huang and A. Yu, *Electrochim. Acta*,2011,**56**,4065-4069.

47. D. Luo, G. Li, X. Guan, C. Yu, J. Zheng, X. Zhang and L. Li, *J. Mater. Chem. A*,2013,**1**,1220-1227.

Figure Captions

Table 1 Results of the Rietveld refinement for z0, z2, z4, z10

Fig.1 Ball-and-stick model of a super cell in $Li_{1.2}Ni_{0.2}Mn_{0.6}O_2$ with a Li^+/Ni^{2+} replacement ratio of 2%

Fig.2 SEM images of specimens z0 (a), z2 (b), z4(c), and z10 (d). The inset on the top right and bottom left of each image are their correspondent magnification image and particle size distribution histogram.

Fig.3 (a) XRD patterns of the specimens z0, z2, z4, z10; (b) (c) magnifications of the dotted boxes denoted in (a)

Fig.4 (a) Plots of magnetic susceptibility and the reciprocal magnetic susceptibility (inset) for specimens z0, z2, z4, z10 and (b) its plots of the magnetization M(H) at 4K

Fig.5 HRTEM images for specimen z0 (a), z2 (b), z4 (c), z10 (d); DF-STEM of specimen z0 (e); atom level EELS for atom marked by the blue (f) and yellow (g) circles in Fig.5(e). The insets on the top right of (a) ~ (d) are the contrast profile of the atom columns denoted by red dotted boxes in transition metal layers.

Fig.6 SAED patterns taken along the $[1\dot{1}0]$ zone axis for specimen z0(a), z2(b), z4(c), z10(d). The miller indexs are denoted according to the $R\bar{3}m$ space group (red) and the C2/m space group(green)

Fig.7 SAED patterns taken along the $[100]_{hex}$ zone axis for the specimen z0(a), z2(b), z4(c), z10(d) and corresponding Schematic diagrams of the diffraction spots z0(e), z2(f), z4(g), z10(h). The miller index are denoted according to the $R\bar{3}m$ space group. The modulation with a wave veter of $\vec{\mathbf{q}} = (0\bar{1}1)$.

Fig.8 (a) EELS patterns of the specimens z0, z2, z4, z10; (b) Enlarged view of Mn L_3 edge and Mn L_2 edge.

Fig.9 (a) Typical initial charge and discharge plots and correspondent coulombic efficiency during the first cycle (inset), (b)Specific charge(closed) and discharge capacity(open) as a function of cycle number, (c)Rate capabilities of batteries at rate ranging from 0.05C to 2C, (d) Normalized discharge capacity values for specimens z0, z2, z4, z10.

Fig.10 (a) Nyquist plot for specimens z0, z2, z4, z10, (b) plot of z' (real part of impedance) against $\omega^{-1/2}$

Table 1 Results of the Rietveld refinement for z0, z2, z4, z10

	a/Å	c/Å	c/a	$I_{(003)}/I_{(104)}$	Zoxy	S_{TMO2}	I_{LiO2}	Ni^{2+}(3b)	Ni^{2+}%	Rwp(%)
z0	2.8588	14.2547	4.9863	1.787	0.2427	2.578	2.168	0.0320	16.0%	7.80
z2	2.8581	14.2538	4.9870	1.812	0.2428	2.582	2.170	0.0249	13.1%	8.06
z4	2.8575	14.2510	4.9872	1.965	0.2432	2.569	2.181	0.0213	11.8%	8.08
z10	2.8533	14.2436	4.9919	1.870	0.2426	2.585	2.163	0.0108	7.2%	7.40

S_{TMO2} is the spacing of the oxygen-metal-oxygen, S_{TMO2} =2(1/3-Zoxy)×c; I_{LiO2} is the spacing of the oxygen-lithium-oxygen, I_{LiO2} =c/3-$S_{TMO2;}$ Ni^{2+}% = Ni^{2+}(3b)/Ni^{2+}(total)

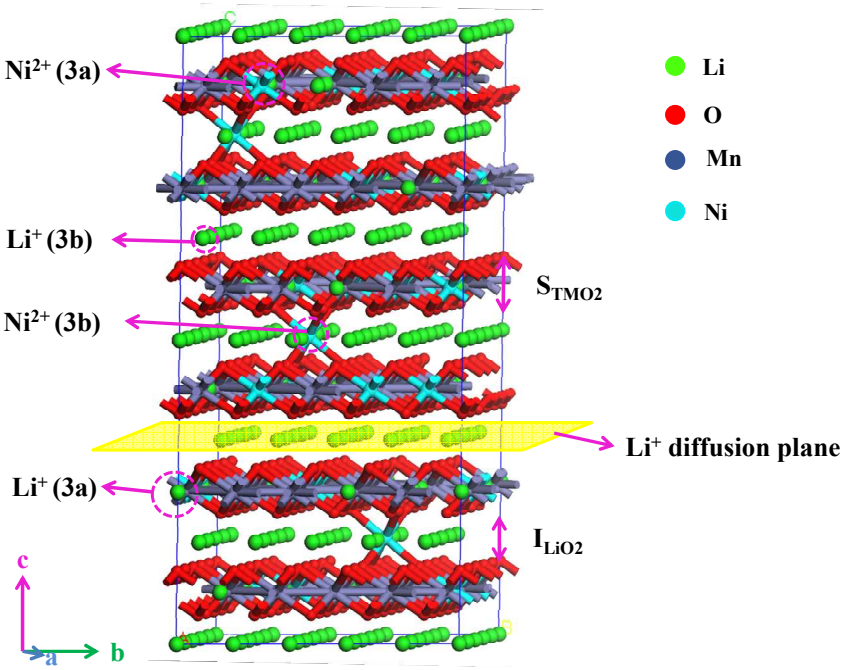

Fig.1 Ball-and-stick model of a super cell in $Li_{1.2}Ni_{0.2}Mn_{0.6}O_2$ with a Li^+/Ni^{2+} replacement ratio of 2%

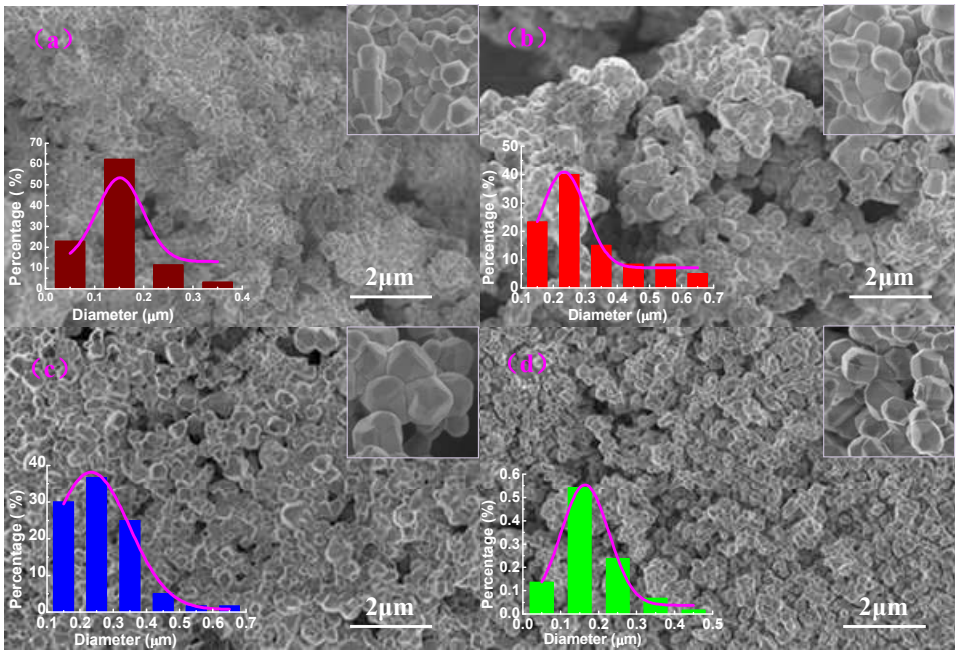

Fig.2 SEM images of specimens z0 (a), z2 (b), z4(c), and z10 (d). The inset on the top right and bottom left of each image are their correspondent magnification image and particle size distribution histogram.

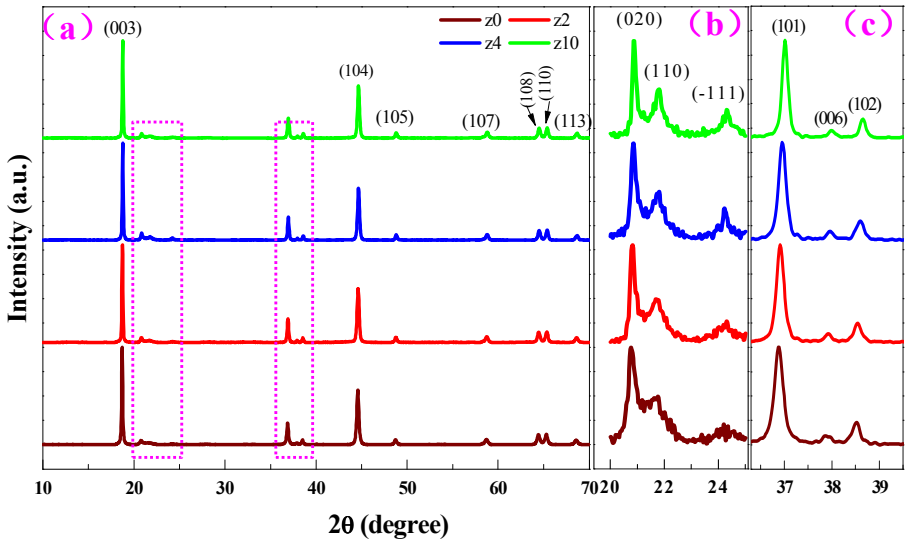

Fig.3 (a) XRD patterns of the specimens z0, z2, z4, z10; (b) (c) magnifications of the dotted boxes denoted in (a)

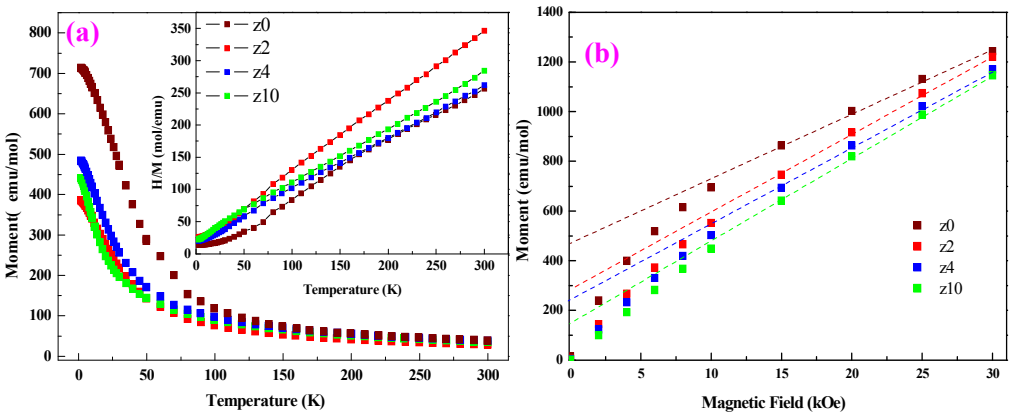

Fig.4 (a) Plots of magnetic susceptibility and the reciprocal magnetic susceptibility (inset) for specimens z0, z2, z4, z10 and (b) its plots of the magnetization M(H) at 4K

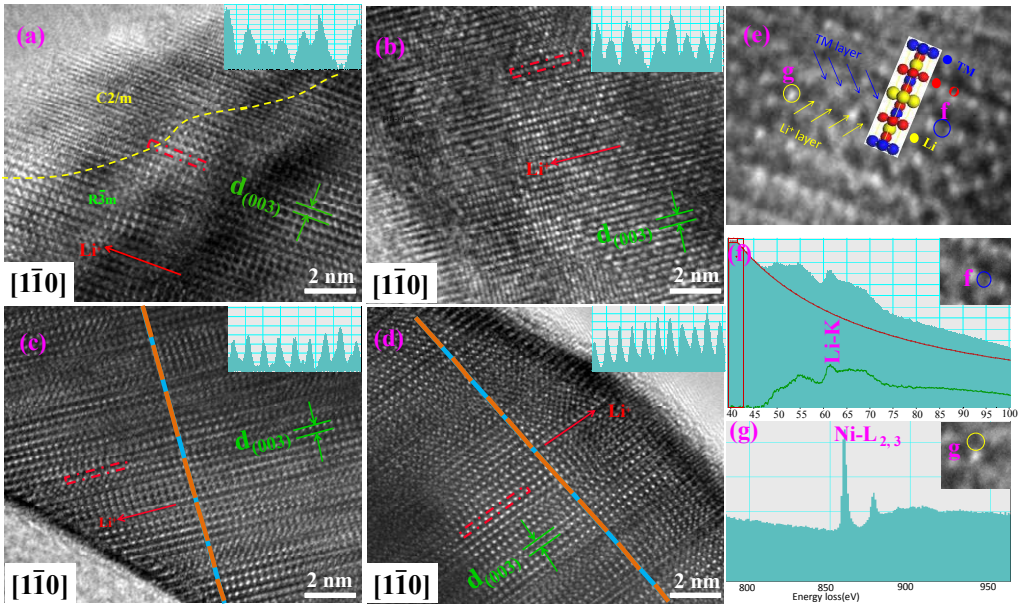

Fig.5 HRTEM images for specimen z0 (a), z2 (b), z4 (c), z10 (d); DF-STEM of specimen z0 (e); atom level EELS for atom marked by the blue (f) and yellow (g) circles in Fig.5(e). The insets on the top right of (a) ~ (d) are the contrast profile of the atom columns denoted by red dotted boxes in transition metal layers.

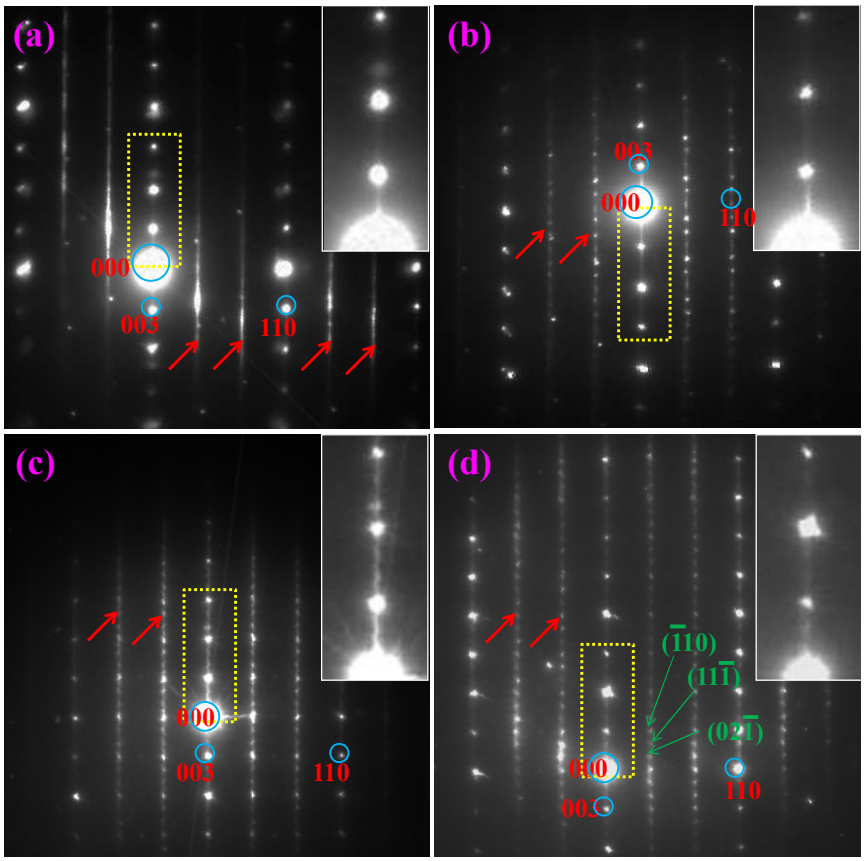

Fig.6 SAED patterns taken along the [1$\bar{1}$0] zone axis for specimen z0(a), z2(b), z4(c), z10(d). The miller indexs are denoted according to the R$\bar{3}$m space group (red) and the C2/m space group(green)

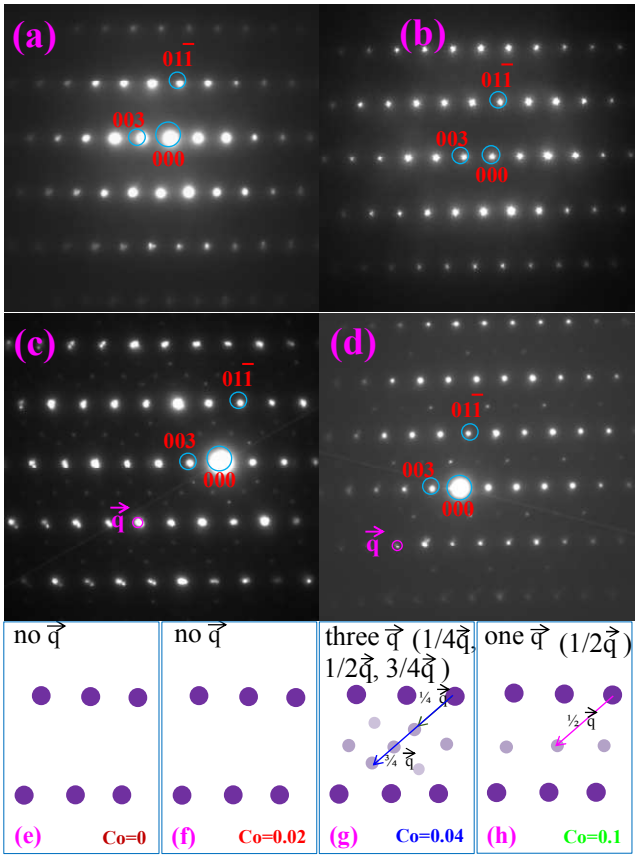

Fig.7 SAED patterns taken along the $[100]_{hex}$ zone axis for the specimen z0(a), z2(b), z4(c), z10(d) and corresponding Schematic diagrams of the diffraction spots z0(e), z2(f), z4(g), z10(h).The miller index are denoted according to the $R\bar{3}m$ space group. The modulation with a wave veter of $\vec{\mathbf{q}} = (0\bar{1}1)$.

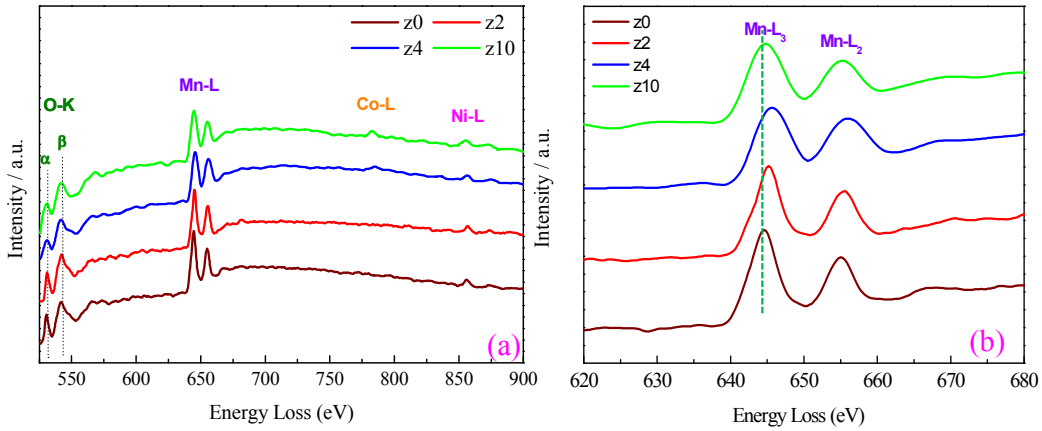

Fig.8 (a) EELS patterns of the specimens z0, z2, z4, z10; (b) Enlarged view of Mn L_3 edge and Mn L_2 edge.

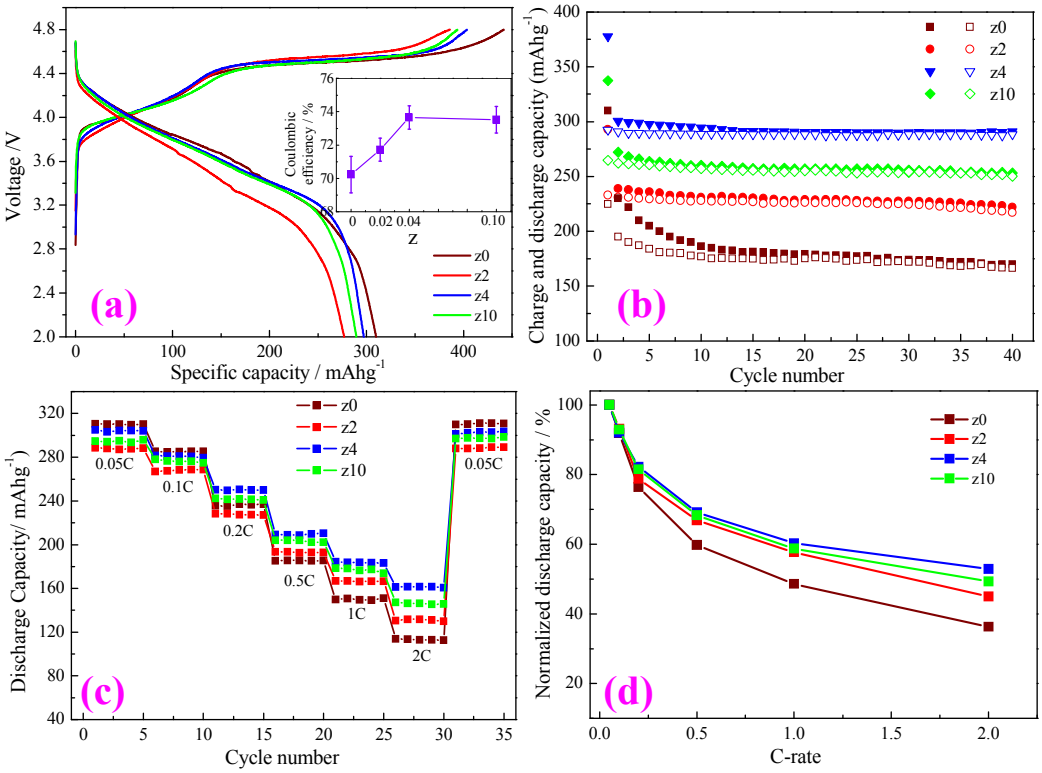

Fig.9 (a) Typical initial charge and discharge plots and correspondent coulombic efficiency during the first cycle (inset), (b)Specific charge(closed) and discharge capacity(open) as a function of cycle number, (c)Rate capabilities of batteries at rate ranging from 0.05C to 2C, (d) Normalized discharge capacity values for specimens z0, z2, z4, z10.

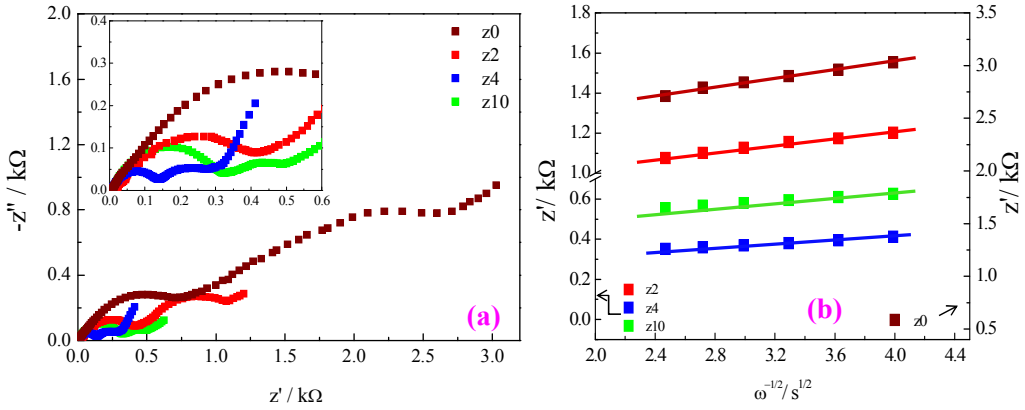

Fig.10 (a) Nyquist plot for specimens z0, z2, z4, z10, (b) plot of z' (real part of impedance) against $\omega^{-1/2}$

Abstract

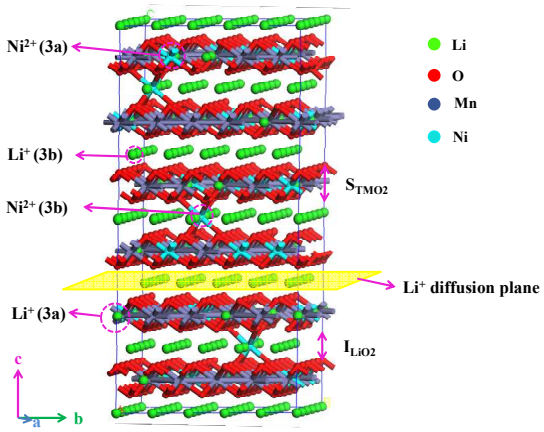

The influences of the Li^+/Ni^{2+} replacement modulated by minor Co dopant on cyclic capacity and rate performance of lithium-rich cathode material $Li_{1.2}Ni_{0.2-z/2}Mn_{0.6-z/2}Co_zO_2$ (z=0, 0.02, 0.04, 0.10) were investigated from the microstructural point of view by comprehensive techniques of high-resolution transmission electron microscopy (HRTEM) imaging, atomic-resolution electron energy loss spectroscopy (EELS), selected-area electron diffraction (SAED), and X-ray diffraction (XRD). It is found that Co played a vital role in decreasing the Li^+/Ni^{2+} replacement ratio in the hexagonal layered $Li_{1.2}Ni_{0.2-z/2}Mn_{0.6-z/2}Co_zO_2$ ($R\bar{3}m$), which is closely related to the electrochemical performance. An evident cationic ordering in the transition metal layers and stacking sequence vertical to the Li^+ diffusion orientation were observed from $Li_{1.2}Ni_{0.2-z/2}Mn_{0.6-z/2}Co_zO_2$ (z>0) system rather than $Li_{1.2}Ni_{0.2}Mn_{0.6}O_2$ system. Compared with $Li_{1.2}Ni_{0.2}Mn_{0.6}O_2$, $Li_{1.2}Ni_{0.18}Mn_{0.58}Co_{0.04}O_2$ showed excellent electrochemical performance with discharge capacity increased to 288.3 $mAhg^{-1}$ from 166.3 $mAhg^{-1}$, capacity retention improved to 98.6% from 73.9% at a current density of 0.1C after 40 cycles, and capacity enhanced to be 161.4$mAhg^{-1}$ from 113 $mAhg^{-1}$ at a higher rate of 2C. The largest interlayer spacing(0.218 nm of O-Li-O layer), highest component of Mn^{4+} ion and the most remarkable superstructure diffraction spots were found from $Li_{1.2}Ni_{0.18}Mn_{0.58}Co_{0.04}O_2$ instead of other specimens confirmed by XRD refinement, EELS, HRTEM, and SAED. Three superstructure vectors modulated by $1/4\vec{\mathbf{q}}$, $2/4\vec{\mathbf{q}}$, $3/4\vec{\mathbf{q}}$ ($\vec{\mathbf{q}}$ =[$0\bar{1}1$]) were simultaneously observed from $Li_{1.2}Ni_{0.18}Mn_{0.58}Co_{0.04}O_2$, indicating a high-degree ordering. Our findings might shed new insights into the understanding of the Li^+/Ni^{2+} replacement by doping minor amount of Co for optimizing the electrochemical performance in Li-ion batteries cathode material from the microstructural point of view.